AIAA AVIATION Forum
17-21 June 2019, Dallas, Texas
AIAA Aviation 2019 Forum

10.2514/6.2019-3598

Aerodynamic and Transition Analysis of the Hybrid Laminar Flow Control Wing Experiment at the ARA Wind Tunnel

Andrea Ciarella*, Simon Lawson† and Peter Wong‡
Aircraft Research Association Ltd., Bedford, MK41 7PF, United Kingdom

Shahid Mughal§
Imperial College London, South Kensington Campus, London, SW7 2AZ, United Kingdom

This paper presents the work undertaken to evaluate the result of the Hybrid Laminar Flow Control (HLFC) test campaign performed in the Aircraft Research Association (ARA) transonic wind tunnel. The transition location was extracted from Infra-Red images at a range of angles of attack and Mach number. Experimentally measured pressure data were also acquired and interpolated to provide input to the laminar boundary layer code, the output of which was used for the stability calculations. The first aim of this paper is to assess the use of stability analysis in conjunction with wind tunnel data and to analyse these results. During the analysis, it was noticed that there exist critical cases in which stability analysis provides an unexpected very low N-factor. It is suggested that the gradients of the pressure distribution determines these critical cases. The calculated N-factor distribution demonstrates that it is not possible to use a single critical N-factor for transition prediction in wind tunnel environment. The second aim of this paper is to assess the effect of suction on transition location and the differences between constant and variable porosity. It is shown that variable porosity has an advantage over constant porosity in terms of required suction pressure and mass-flow.

I. Nomenclature

c	=	Chord
Cd	=	Drag Coefficient
Cp	=	Pressure Coefficient
d	=	Porous hole diameter
HLFC	=	Hybrid Laminar Flow Control
LE	=	Leading Edge
M	=	Mach Number
NLF	=	Natural Laminar Flow
Ψ	=	Wave angle
LST	=	Linearised Local Stability Theory
LPSE	=	Linearised Parabolised Stability Equations
p_{ext}	=	External Pressure
p_{plenum}	=	Plenum Pressure
μ	=	Local air dynamic viscosity
t	=	Porous panel thickness
V_h	=	Hole Velocity
S-G	=	Savitzky-Golay
T	=	Temperature
TE	=	Trailing Edge
TRL	=	Technology Readiness Level
$T-S$	=	Tollmien-Schlichting

*Senior Aerodynamics Engineer, Aerodynamic Capability, aciarella@ara.co.uk
†Senior Aerodynamics Engineer, Aerodynamic Capability, slawson@ara.co.uk
‡Technical Consultant, Aerodynamic Capability, pwong@ara.co.uk
§Lecturer, Departments of Mathematics, s.mughal@imperial.ac.uk

α_i = Spatial amplification rate in the complex wavenumber $\alpha = \alpha_r + i\alpha_i$
β = Spanwise wavenumber, where the spanwise wavelength $\lambda = 2\pi/\beta$

II. Introduction

In recent times the main drive of the transport aircraft industry is the reduction on the environmental impact of aircraft. With the help of the European Clean Sky and Horizon 2020 programmes, the industry is focusing on designs that can be considered a game changer in terms of reducing emissions. Among these designs, natural laminar flow (NLF) and hybrid laminar flow control (HLFC) are technologies which have the potential to significantly reduce fuel burn and engine emissions of future aircraft.

Several research projects have been carried out over the past years to develop computational tools and design methodologies to enable aerodynamic design of laminar flow wings. An essential part of maturing this technology to higher Technology Readiness Level (TRL) is to generate data that allows the validation of modern tool-sets. Aircraft Research Association (ARA) has been involved in laminar flow research for many years, both in developing analysis methodologies for CFD calculations and in wind-tunnel testing technique. In recent years, emphasis has been on developing wind-tunnel test techniques for detecting transition for NLF and HLFC configurations, Refs [1], [2] and [3] are examples of the work carried out at ARA. The design and performance analysis of an alternative HLFC concept with a single chamber and variable porosity surface for a civil transport aircraft has also been carried out at ARA in Ref. [4] , while an example of a military aircraft application is that presented in Ref. [5]. These papers demonstrate the possibility of controlling transition with the use of appropriate variations in the hole spacing to hole diameter ratio, hole diameter and skin thickness.

This paper presents the analysis of the results of the wind tunnel test described in Ref. [3] using linear local stability (LST) and contrast the findings with the more physically correct linear parabolised stability equations (LPSE) analysis [6, 7]. The experimental arrangement is presented in Fig. 1. This schematic shows the wing at the sweep angle of 35°. The wing has a constant section across the span. In this figure we can see the cartridge, the thermal insulating panel, the pressure taps, the hot-films and the wake rake used for drag measurement. The fuselage was designed to provide minimum interference with the wing.

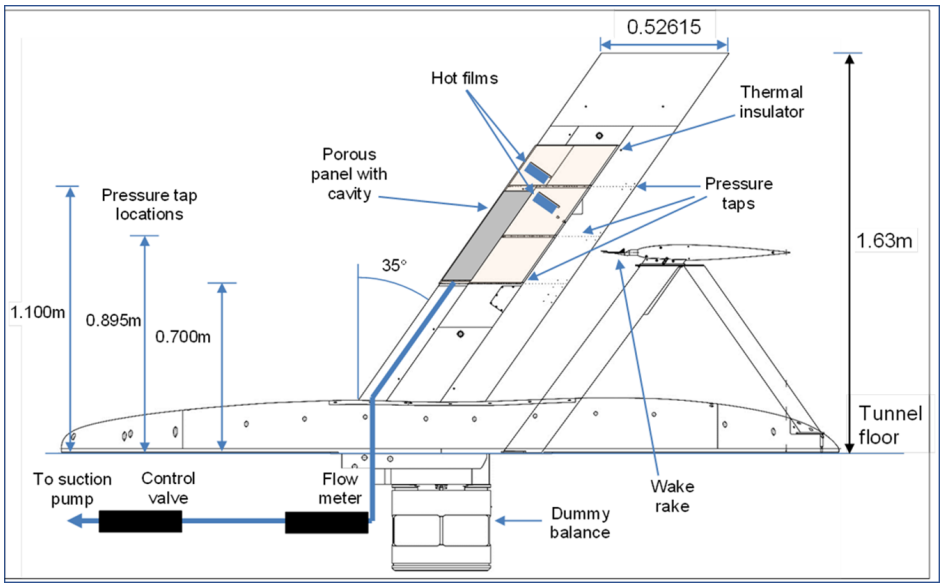

Fig. 1 Experimental arrangement for the HLFC wind tunnel test performed in ARA Transonic Wind Tunnel

The wing section is presented in Fig. 2, which shows the schematic of the porous panel and location of the thermal insulator. The porous panels had 45 μm diameter holes, providing porosity from the leading edge to 20% of the chord on the upper surface. The constant porosity panel had a hole spacing to hole diameter ratio of 12, while the variable porosity panel had a linear variation of hole spacing to hole diameter ratio from 12 at the LE to 8 at 5% chord and

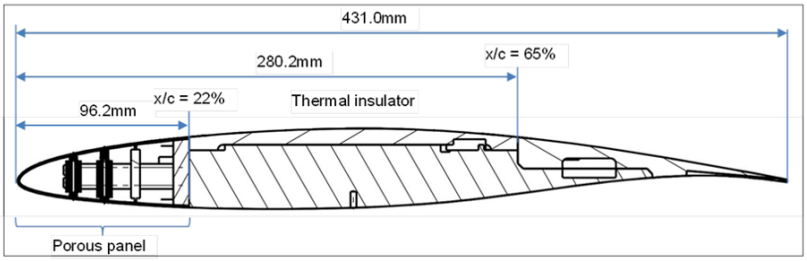

Fig. 2 Sectional view of the wing normal to leading edge

returning back to 12 at 20% chord, as shown in Fig. 3. The constant porosity panel had a total of 136,964 holes and the variable porosity panel a total of 206,113 holes.

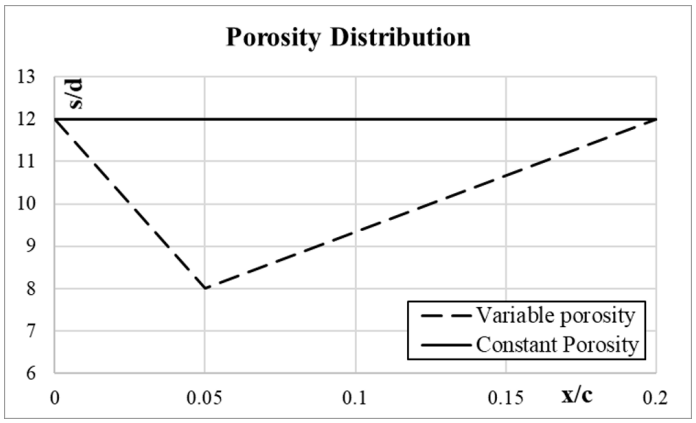

Fig. 3 Hole spacing to diameter distribution for the variable and constant porosity cartridges

III. Analysis methodology

The most widely used method to estimate transition location for aircraft configuration applications is called the e^n method; it was presented in 1956 in two different reports [8] and [9]. This method neglects the receptivity process, which describes how instabilities are essentially generated in the boundary-layer; the method also does not account for the non-linear breakdown to turbulence. It considers that if the growth of any wave amplitude exceeds some large factor the non-linear behaviour is assumed to cause breakdown to turbulence. Consider a disturbance of frequency ω_0 and spanwise wavenumber β propagating downstream (see Fig. 4(a)). This wave passes the stable region till x_0 then it amplifies till x_1 and it is damped thereafter, as shown in the Fig. 4(b). If we call A_0 the amplitude at the neutral point x_0, and A the amplitude at another location after the stability point we can define:

$$\frac{A}{A_0} = e^{\int_{x_0}^{x} -\alpha_i dx} \tag{1}$$

$$log_e \frac{A}{A_0} = \int_{x_0}^{x} -\alpha_i \, dx \tag{2}$$

Figure 4(b) shows the evolution of this disturbance in terms of the value defined above. The envelope of the curves, for all frequencies ω taking the maximum value at each x location is called the N-factor envelope. It is defined as:

$$N = \max_{\omega} \frac{A}{A_0}; \tag{3}$$

the so-called envelope of envelopes thus follows by maximizing this expression over all spanwise β wavenumbers too in addition to the entire unstable ω parameter space, i.e.

$$N = \max_{\beta} \max_{\omega} \frac{A}{A_0}. \tag{4}$$

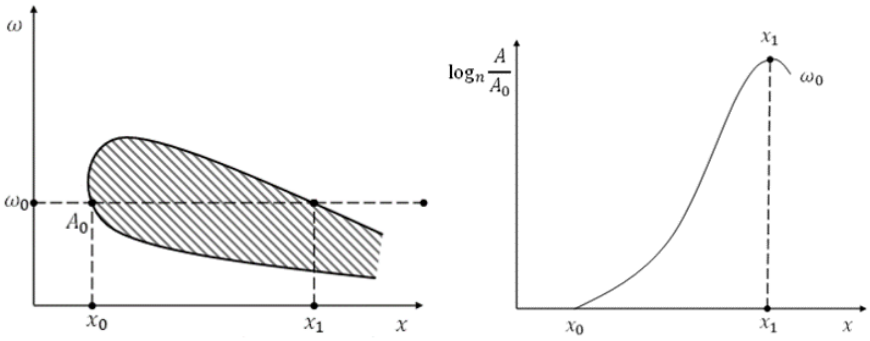

(a) Eigenvalues chart in complex ω space (b) Integration methodology

Fig. 4 N-factor wave evolution in the boundary layer

In most applications, linear stability theory is used to calculate the eigenvalues of the system. This is because the distance between the end of the linear region and the breakdown to turbulence is short compared to the extent of the linear region, hence secondary/non-linear mechanisms can be ignored. The shortcomings of the linear methods, without, for now, going into too much detail, already alluded to above are:

- Role of the freestream environment and hence receptivity is not considered;
- Non-linear mechanisms are not modelled.

A more modern approach that allows the incorporation of weakly non-linear effects is the non-linear parabolised stability equations PSE [6, 7]. The method includes:

- Modelling exponential growth through primary and higher order interaction of disturbances;
- Non-parallel and surface geometrical effects (i.e. curvature) in a unified manner;
- Initial conditions, derived from receptivity analysis may be used to force nonlinear evolution (see Ref. [10], [11]).

Despite these limitations the LST method is widely used in the aerospace industry; primarily due to its simplicity and in truth the free-stream environment, receptivity and non-linear modelling are still topics in some infancy from an end-use engineering fidelity and physics modelling viewpoint. The partly unknown and uncontrollable nature of the freestream turbulence and acoustic forcing environment in wind-tunnels as well as uncertainties in the surface roughness finishing standards in model preparation, are key aspects which require to be included in a truly physics based method of transition prediction. The success of the e^n method, which may be used both with LST and linear PSE analysis is due to speed and accuracy. The methodology provides reasonably accurate estimations of the transition location required to successfully design aircraft with extended regions of laminar flow. A vast database of correlations, dependent upon wind-tunnel facility and free-flight have been built up over the years, primarily based on the LST model. PSE based correlation databases are not as extensive as those based on LST, due still to the novelty of the PSE model despite 25 years having elapsed since its development [6]. The physics correctness of PSE models over LST is now universally accepted. In some quite recent detailed analysis (see Ref. [12], [13]) linear PSE results are shown to be in agreement with direct solutions to the more *exact* linearised Navier-Stokes simulations for flows without and with small portions of locally reversed flow too.

This paper is concerned with critically evaluating the use of linear stability analysis tools comprising LST and LPSE models, and correlation of observed transition fronts with results derived from the two quite radically different theories. The laminar-turbulent transition front was determined through observations using the Infra-Red (I-R) imaging of the experimental test points. The methodology is the same as used in Ref. [2]. It uses the Savitzky-Golay algorithm [14] to determine transition onset and completion. An example of this process is presented in Fig. 5. Fig. 6(a) presents a crop of the I-R image, the black line represents the measurement line used in this example. This line produces the original signal line in Fig. 5(b). A noisy curve is extracted then smoothed using the S-G algorithm and first and second derivatives are

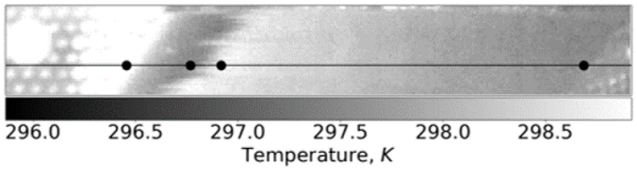

(a) Infra-Red Image

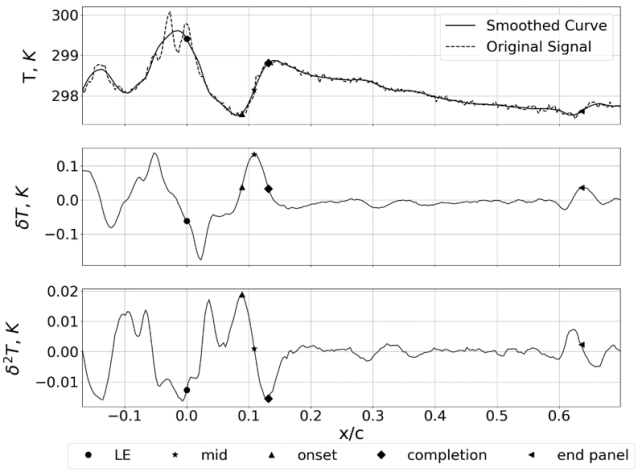

(b) Signal evaluation

Fig. 5 Example of the transition extraction technique used in HLFC

computed from the smoothed curve. A semi-automatic algorithm * is then used to determine the important features and points :

- LE: leading edge of the curve;
- Mid: location of the mid point between onset and completion;
- Onset: transition onset;
- Completion: transition completion;
- End panel: location of the measurement panel.

The transition mid-point is defined as the local maximum of the first derivative of the smoothed data. The second derivative provides information regarding the onset (local maximum) and the completion (local minimum). This approach allows the selection of multiple spanwise sections, the average of this data is the extracted transition location. At the end of the calculation and analysis stage, the local N-factor derived from the stability analysis was correlated with the Infra-Red inferred tunnel transition images.

The input data used for the infinite swept (so-called 2.5D) stability calculation is as follows:

- Sectional geometry as inspected with ARA's optical scanner;
- Experimental flow conditions: Temperature, Reynolds and Mach number;
- Appropriately smoothed and cleansed experimentally measured surface pressure data.

The tools used to perform the calculations are as follows:

- A compressible boundary layer code used was Ref. [15].
- The tool used was a linear stability code (Ref. [16]).
- The tool used for LPSE was Ref. [17, 18].

It is important to note that we use the experimentally measured pressure data, as the input for the subsequent evaluation of the laminar boundary-layer profiles, with the codes described above[15, 18].

*Semi-automatic means that an initial guess of the transition location, leading-edge (LE) and end panel is required to extract the correct transition location

A. Effect of small pressure variations on the boundary layer analysis

During the analysis using linear PSE and non-linear PSE, smoothing operations were performed on the pressure distribution for the subsequent boundary-layer computations, these smoothing exercises did not have an impact on the instability analysis using linear stability analysis. Small variations of the pressure distribution due to different test runs were also considered, also the variations on the N-factor plots were negligible. In most cases the results computed with the raw experimentally measured data (comprising 54 pressure taps) and more refined pressure data obtained upon subsequent smoothing and interpolation procedures (261 boundary-layer computational points), produced nearly identical boundary-layer solutions and instability results (see, the green, red and blue curves in Fig. 6(a)).

In some data sets however, the occurrence of non-smooth pressure distribution fluctuations arising from experimental noise, can be seen in Fig. 6 (e.g. data set C133). A small surface pressure spike arises in the measurements at $x/c \sim 0.5$, which causes the boundary layer solver to fail at that point, by way of the numerics predicting a sharp drop in the streamwise skin-friction Cfx – this point would nominally be taken to herald the laminar separation onset due to the adverse pressure gradient there. However removal of this pressure point and a re-computation of the boundary-layer solution then predicts a radically different behaviour and the laminar boundary-layer computations proceed to nearly $x/c \sim 0.6$ as opposed to the earlier $x/c \sim 0.5$ termination point. Considering the friction coefficient Cfx extracted from the boundary layer tool (blue line) it is clear that this spike destabilizes the numerical algorithm leading the code to stop at that location. This may lead to the conclusion that at that location transition is due to laminar separation. Although this conclusion appears reasonable it is important to notice that removing this spurious point stabilizes the computations, which then allows boundary layer computations to successfully proceed to a further downstream position where "laminar separation" is predicted to occur beyond 60% chord. The right side of the picture shows the differences between the two cases in terms of the calculated N-factor envelope. The main differences arise after 50% chord where the solution calculated without the surface pressure spike shows a significant increase in the N-factors envelope.

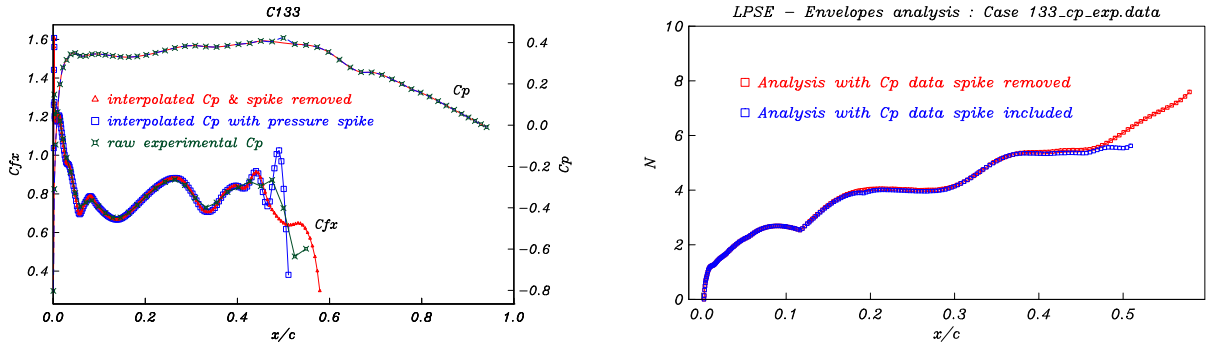

(a) Pressure distribution with a pressure tap spike and effect on the predicted laminar flow streamwise skin friction Cfx.

(b) LPSE calculations with and without the pressure tap spike

Fig. 6 Simple case in which the presence of a spurious pressure tap spike in the surface pressure distribution may lead to different solutions in the boundary layer code

The I-R image observed experimental transition was at the location of the spike leading the authors to believe it was a standard laminar separation case or breakdown due to the presence of a bubble but:

- The flow on top of the pressure taps was fully turbulent due to the presence of wedges in that region
- The pressure distribution over the entirety of the spanwise wing measurement plane when averaged, it was observed that the spike was not present in all of the spanwise sections.

This particular data set (C133) leads to the conclusion that although laminar separation induced tripping seems a reasonable scenario, it is not possible with this particular data to be absolutely positive of our conviction. The flow develops over a mildly adverse pressure gradient (beyond $x/c \geq 0.5$) with the Cfx values predicted by the boundary-layer computations indicating a sharp reduction in skin-friction, and possibly laminar separation incipient. However N-factors values of 8 are just about attained by $x/c \sim 0.6$, which based on previous experience would suggest that the flow remains laminar up to these positions too.

IV. Stability analysis

A. Solid wing - no suction cases

The first part of the analysis considers the linear stability analysis of the wing when the solid cartridge is used. This is the equivalent of considering a solid wing with 35° sweep and constant section. Fig. 7 shows the variation of the transition location against angle of attack. The black line represents the value of transition at different angles of attack, this point is the transition mid-point extracted from the I-R images. The grey band shows the intermittency region between onset and completion. The transition front starts from 10% at a negative angle of attack, growing to 50% at 0 degree. After reaching a chord-wise maximum at the 0 degree incidence point, it reduces once again at increasing angles of attack.

Using the transition location in Fig. 7, compressible linear stability analysis was used to compute and correlate the N-factor as a function of the angle of attack, this is presented in Fig. 8(a). Unexpectedly, the N-factors correlated with the observed I-R transition front is not constant but varies between 11 and 4, it starts from 11 at negative angle of attack and reduces monotonically until reaching a minimum. After this minimum, it starts to increase again. Looking at Fig. 8(b) the wave angle is ≈ 80 between the angle of attack of -4 and 0, this is an indicator that the type of transition should be of the cross-flow type, while for incidence angles greater than 2 Tollmien-Schlichting (T-S) induced breakdown occurs. In the region between 0 and +2 degrees, the transition mechanism is not clearly defined, we call this oblique wave induced. This behaviour contradicts the standard theoretical approaches used in design, which is nominally based on the assumption that the transition N-factor must be constant (usually $N = 14 \sim 10$ for Crossflow (CF) induced transition and $N \sim 8$ for T-S dominated transition). Figure 9 shows the relation between transition location and N-factor. It is

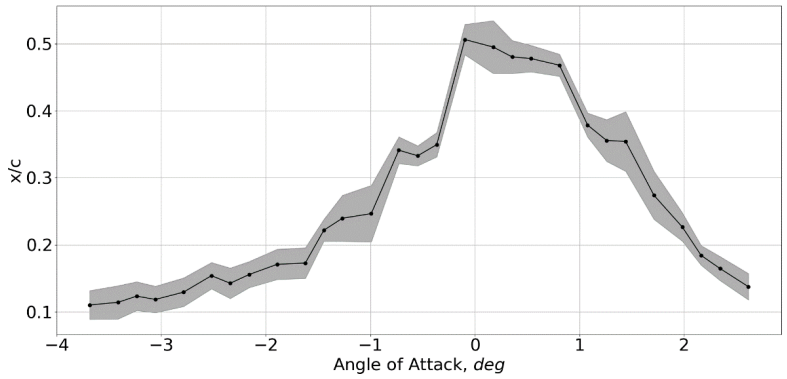

Fig. 7 Infra-Red extracted transition front variation with angle of attack at M=0.7 with the solid cartridge.

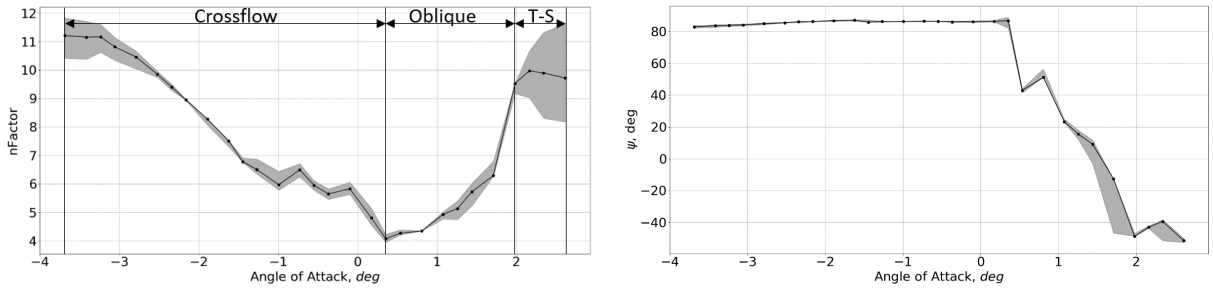

(a) Transition N-factor correlated with I-R

(b) Wave angle at transition location

Fig. 8 Results of the linear stability analysis at M=0.7 with the solid cartridge

noticeable that the correlated N-factors are highest where transition is observed to occur closest to the flow attachment point close to the leading edge, while N-factors tend to get smaller with forward movement of the transition front. The

cause of this mechanism may be due to surface imperfections, secondary mechanisms, tunnel environmental conditions – we strongly believe that a wide plethora of excitation mechanisms exist in the tunnel testing environment, which with varying wing incidence preferentially excite differing disturbances which then dominate the breakdown process. These mechanisms can not be predicted with linear stability. The prediction from linear stability is un-physical/unrealistic in these cases.

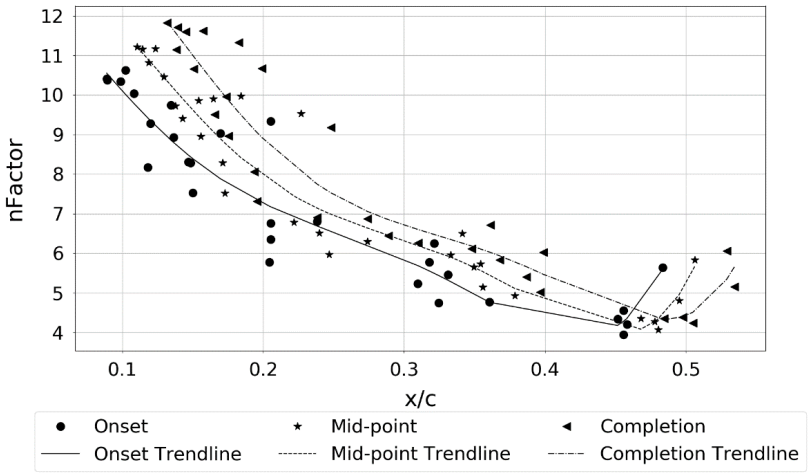

Fig. 9 Transition front movement and correlated N-factor from LST analysis at M=0.7

Figure 10 presents further examples of unexpected predictions of the linear stability analysis. Figure 10(a) presents standard behaviour of linear stability for cross-flow, experimental data places transition at 10% this means that the estimated N-factor is greater than 10. In Fig. 10(b) the transition front varies between 23% to 30%, in this range the N-factor is greater for the shorter transition front – theoretically the implication is that the flow is stabilizing between 23% to 30%. This is un-realistic because there does not appear at face-value to be any mechanism which stabilizes the flow. Linear stability apparently does not provide a useful answer in this case.

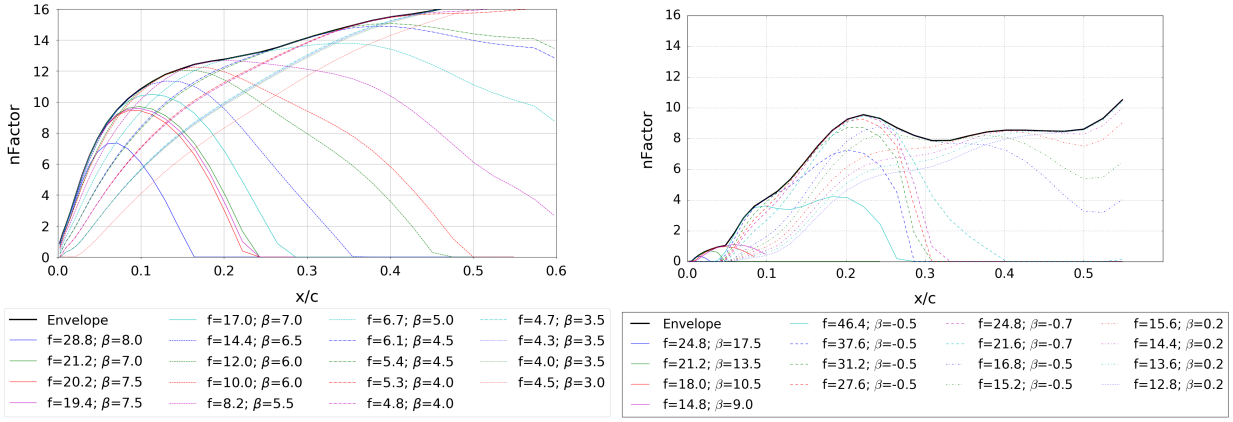

(a) Angle of Attack = −3.06° (b) Angle of Attack = 1.71°

Fig. 10 Linear stability chart of two different angle of attack at M=0.7

1. Incompressible Linear Stability

In the previous section the simulations were performed using a compressible linear stability solver, it is important to see how it compares with an incompressible solver. The N-factor trend seen using the compressible solver is still present using the incompressible modelling as presented in Fig. 11. The scale of the values is slightly different but the overall trend is identical.

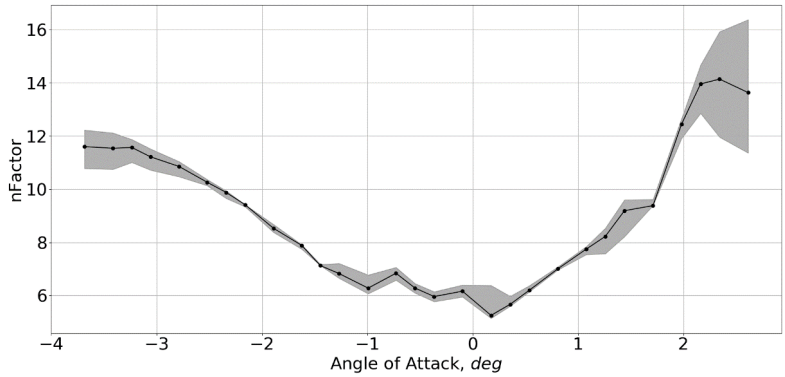

Fig. 11 N-factor using an incompressible linear stability solver

To identify the difference between the compressible and incompressible LST analyses, it is better to output the "N-factor Cross-Flow" NCF curve and "N-factor T-S" curve NTS curve as in Fig's 11 and 12. Three cases are presented at Mach=0.7:

1) Crossflow transition case: Angle of attack = -3.7
2) Interacting waves case: Angle of attack = 0.35
3) Tollmien-Schlichting transition case: Angle of attack = 2.34

Starting from the top of Fig. 11 it is clear that both solvers behave similarly with a clear and distinct transition behaviour. The situation gets complicated in the middle part of the figure, the compressible solver show a flat trend with an extended area of potential crossover between T-S and CF induced transition; the potential for interaction between the T-S and CF disturbances cannot be predicted by linear stability, and would require a nonlinear analysis to be undertaken. The incompressible analysis shows that the two curves interact only at $x/c \sim 0.18$. Both solvers predict a very low N-factor that seems to be unrealistic. In these cases the instabilities appear to persist at low N-factor levels; non-linear effects eventually must become significant to trigger breakdown. Linear stability is thus not suitable to analyze this case and a non-linear method is required. The bottom part of Fig. 11, shows a consistent trend with both solver models, indicating the likelihood of travelling CF dominated transition.

2. Effect of the integration strategies

Standard practice in LST is to carry out the simulation using an integration strategy that keeps the wave number constant during the integration of the computed growth rates. Other approaches keep the wave angle $\Psi = tan^{-1}(\frac{\beta}{\alpha})$ relative to the viscous streamline fixed or the wavelength $\lambda = 2\pi\alpha_r + \beta$ constant. Comparing the N-factor distribution using the standard approach in Fig. 8(a) with the integration strategies described in the previous paragraph, Fig. 13, the general N-factor trend is still there allowing the conclusion that in the cases considered the integration strategy has little bearing on our general findings and conclusions. Figure 14 shows the stability curves evolution for the integration strategies considered at different angle of attack. This shows that the global behaviour is maintained with all the integration strategies.

B. Porous cartridges

The main focus of the HLFC wind tunnel test campaign was to compare the effectiveness of different suction patterns to control transition. Fig. 15 shows the wake rake measured drag variation with changes of the mass flow at different angles of attack. It is clear that there is a reduction in drag due to increasing suction. The reduction of drag can be up to 10 drag counts. The chamber pressure for variable and constant porosity is represented in Fig. 16. In both cases, as expected, a reduction of the mass flow corresponds with a reduction of the chamber pressure. Looking at the example at an angle of attack of 1.63 degrees it is noticeable that to obtain a similar level of mass flow the reduction of the chamber pressure is $\sim$ 2000 Pa in the variable porosity case while it is $\sim$ 5000 Pa in the constant porosity scenario. This proves that variable porosity provides a better control on transition with reduced chamber pressure.

As presented in Ref. [3], the critical design parameters for the HLFC concept are the suction mass flow and the suction velocity distribution required to delay transition. The relationship between the pressure difference across the

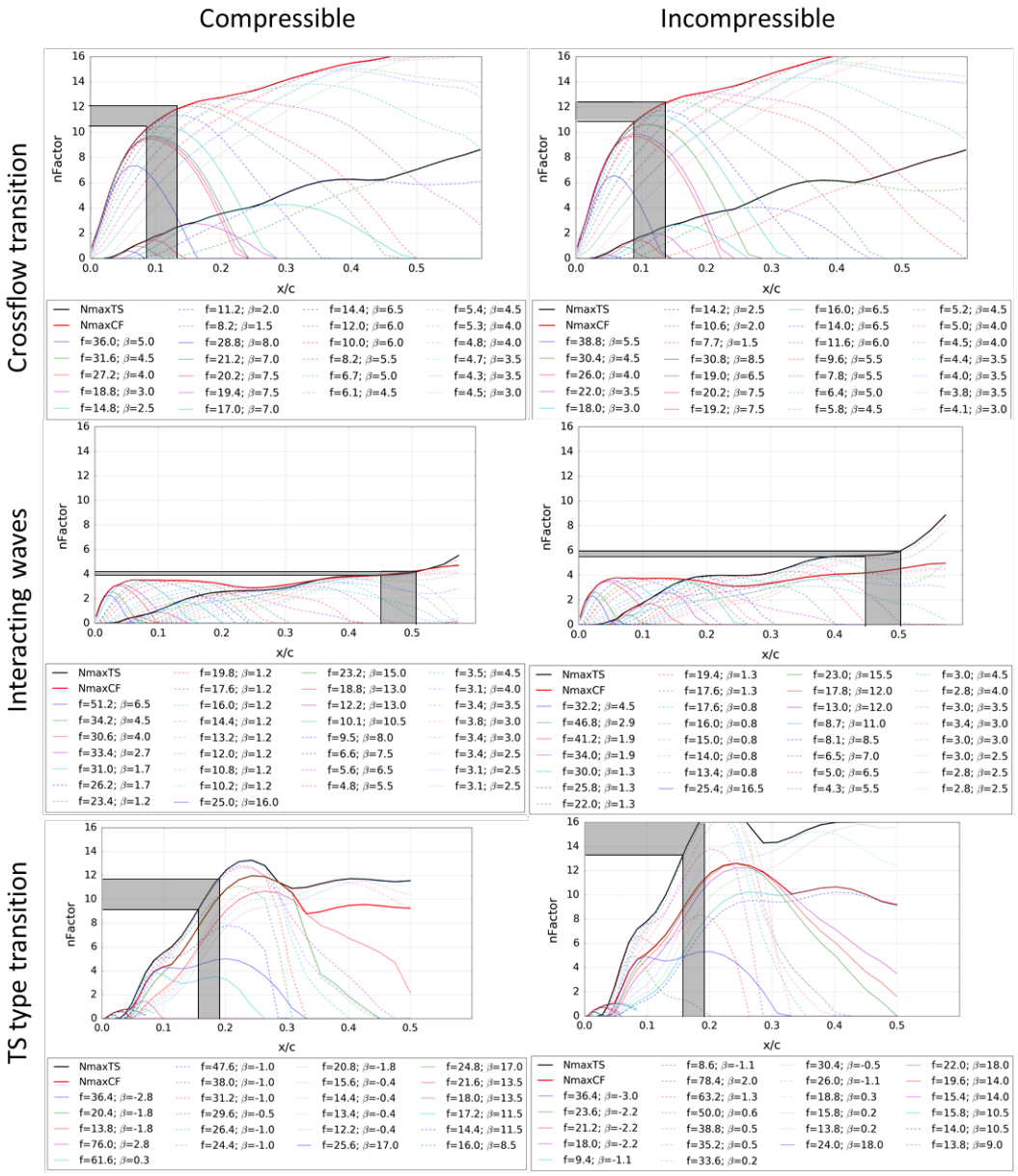

Fig. 12 Difference between compressible and incompressible solver the N-factor calculation (two N-factor approach)

suction hole and suction velocity has been determined in the ARA experiment. This relationship is in a similar form as the empirical relationship defined by Poll et al. [19] and Preist and Paluch [20], namely:

$$p_{ext} - p_{plenum} = \frac{1}{2} A\rho(V_h)^2 + 32B\mu\frac{t}{d^2}V_h \tag{5}$$

The boundary layer solver was modified to account for the suction system and the constants A and B are defined empirically as:

$$A = 1.163 \tag{6}$$

$$B = 0.197 \tag{7}$$

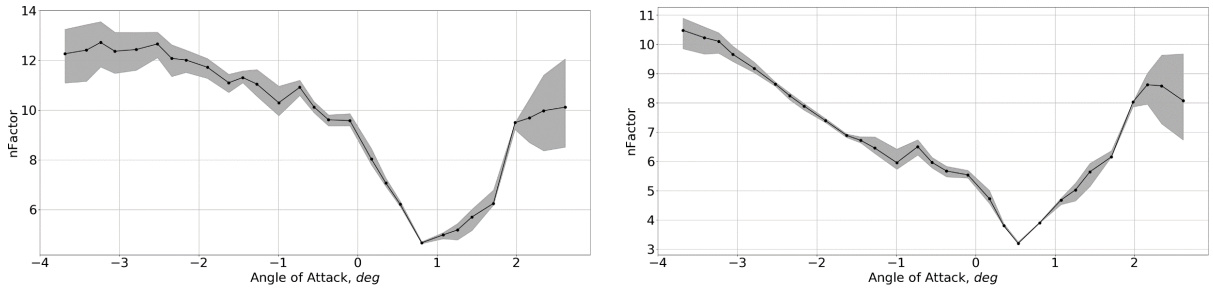

(a) Constant Wave Angle

(b) Constant Wave Length

Fig. 13 Linear stability comparison using different integration strategy

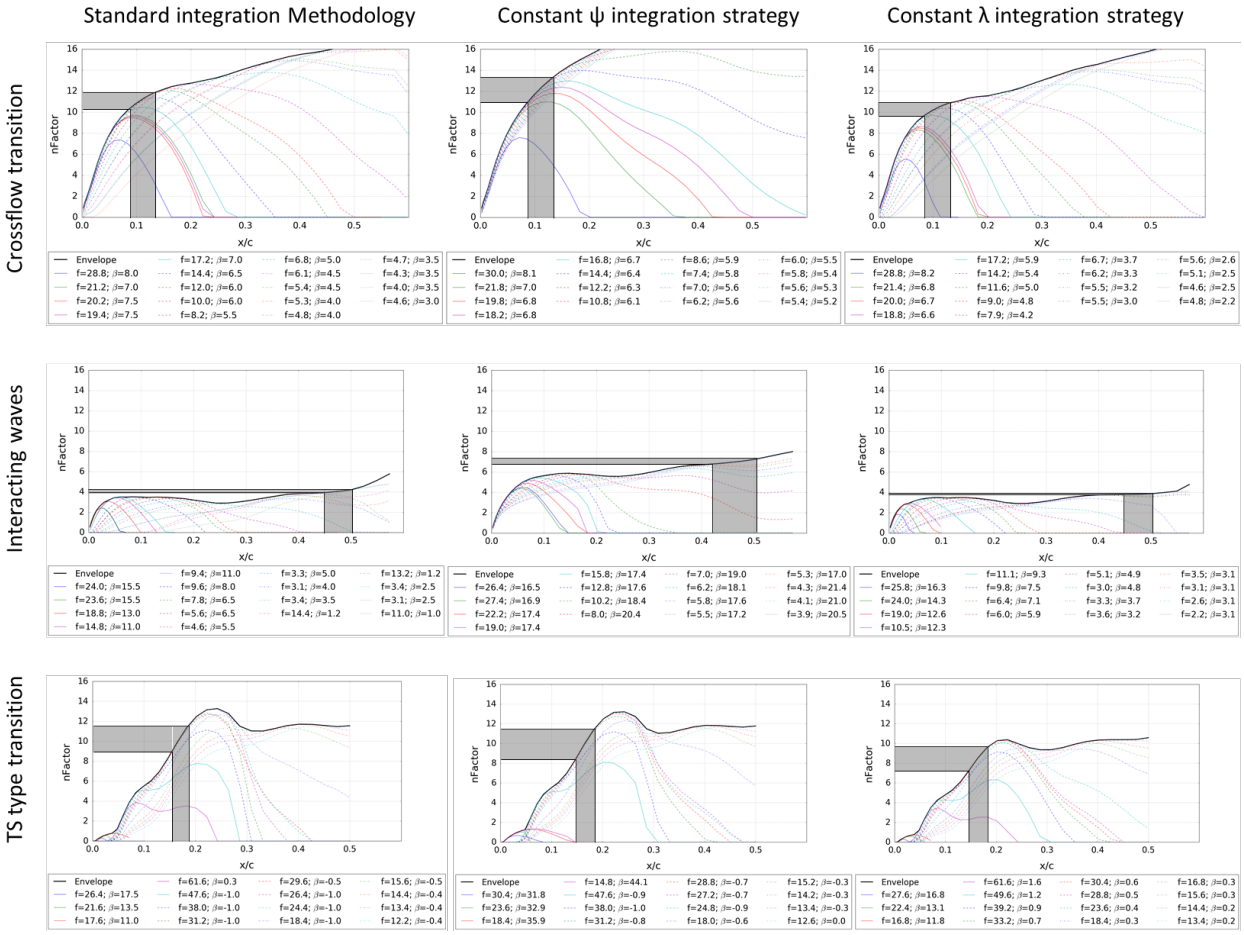

Fig. 14 Linear stability comparison using different integration strategy

The methodology used to experimentally calculate these coefficients is presented in Ref. [3]. The effect of suction as modelled in linear stability is shown in Fig. 17. The solid panel in Fig. 17(a) shows the pressure distribution and the N-factor distribution. If we look now at the effect of suction on the linear stability with constant porosity (Fig. 17(b)) we notice that at maximum suction the variation of pressure between the inside and the outside of the cartridge, Δp, is almost positive everywhere meaning that blowing unlikely to be present. In this case, the effect of the suction is to push down the N-factor curve, lowering the envelope. The same effect can be seen in Fig. 17(c) for the variable porosity.

The main differences between the constant and variable porosity are:

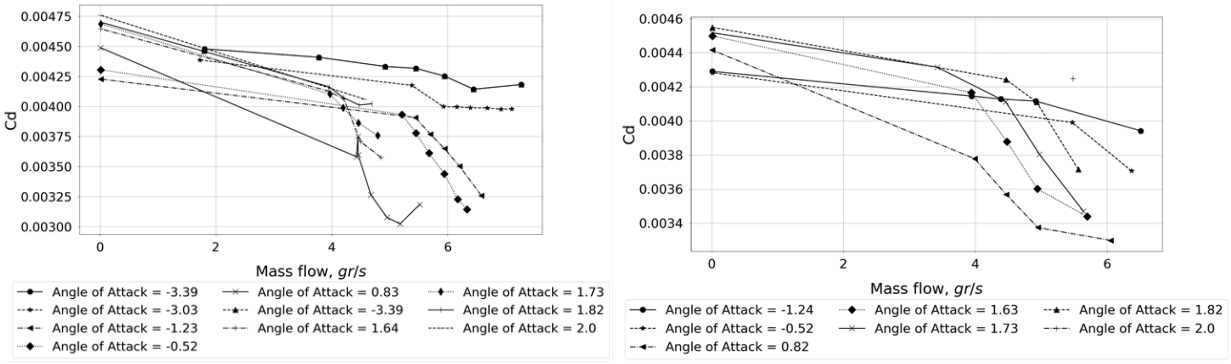

(a) Constant Porosity (b) Variable Porosity

Fig. 15 Effect of mass flow on the drag at M=0.7

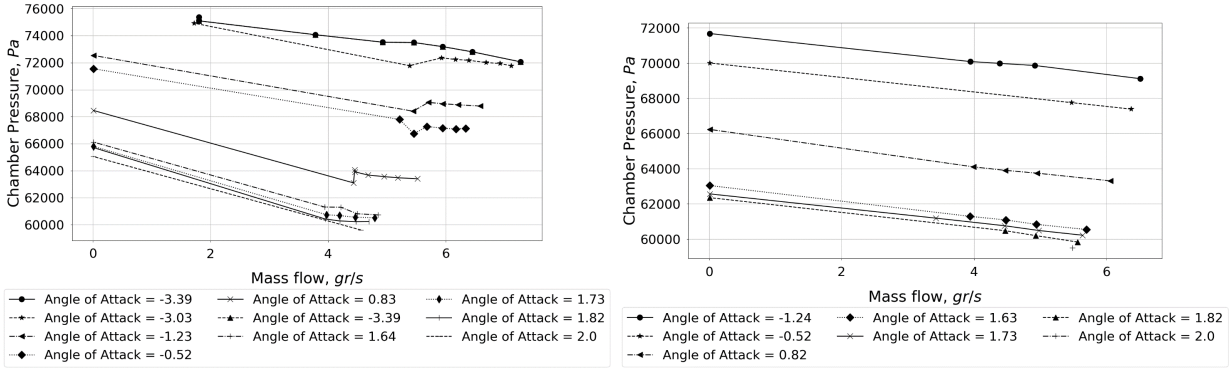

(a) Constant Porosity (b) Variable Porosity

Fig. 16 Relation between chamber pressure and mass flow at M=0.7

- The effect of lowering the N-factor is stronger for constant porosity.
- The suction required for variable porosity to achieve the same mass flow is higher in the variable porosity. The difference in the case presented is ≈ 200 Pa, as shown in Fig. 17

The effect of blowing on transition has also been investigated. The main issue with using suction to stabilise the flow is when the suction system is unable to suck enough and instead the system starts blowing. An example of this problem is the case presented in Fig. 18. In Fig. 20(b) blowing occurs between 2% to 6% chord and causes transition in the porous region. On the other hand for variable porosity (Fig. 18(c)) although, blowing is present, the amount of suction achievable downstream of blowing was able to stabilize the flow delaying transition at 50% chord. This suggests that it may be possible to delay transition even in the presence of blowing, provided there is sufficient suction downstream of blowing. Future work will require to understand the value of this critical N-factor for suction cases. Experimental evidences suggest this value to be lower than the critical N-factor considered in non-suction cases.

C. Comparison between Linear Parabolised Stability analysis and Linear Stability analysis

Preliminary analysis of a few select data sets is presented in Fig. 19, which should be contrasted with Fig. 8(a). The PSE methodology used is performed using the surface curvature correction; the PSE model by its very nature automatically implies that non-parallel effects are included in the N-factors computation. This figure shows a similar trend in comparison with local linear stability analysis with N-factors slightly higher in the LPSE analysis. Looking at Fig. 20 the LPSE trends coincide with those obtained with linear stability theory – this further confirms correctness of the methodology used in both methods due to consistency of results and findings.

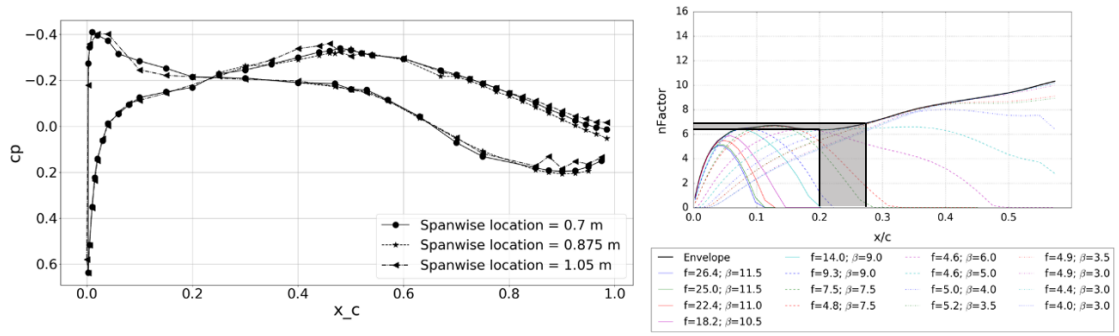

(a) Solid Cartridge

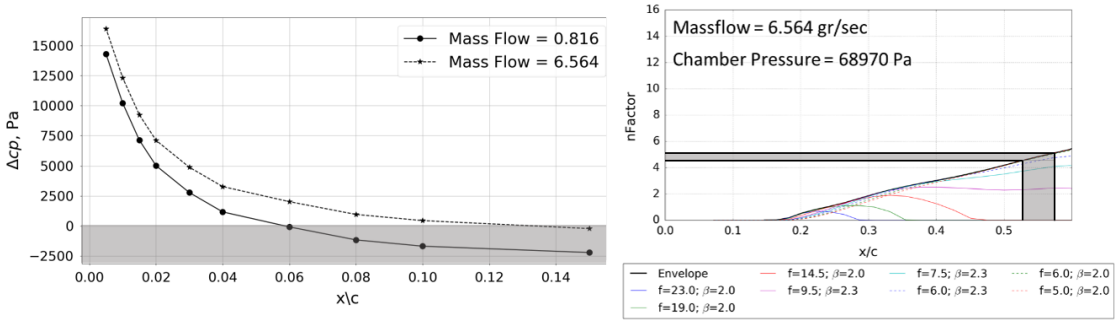

(b) Constant Porosity

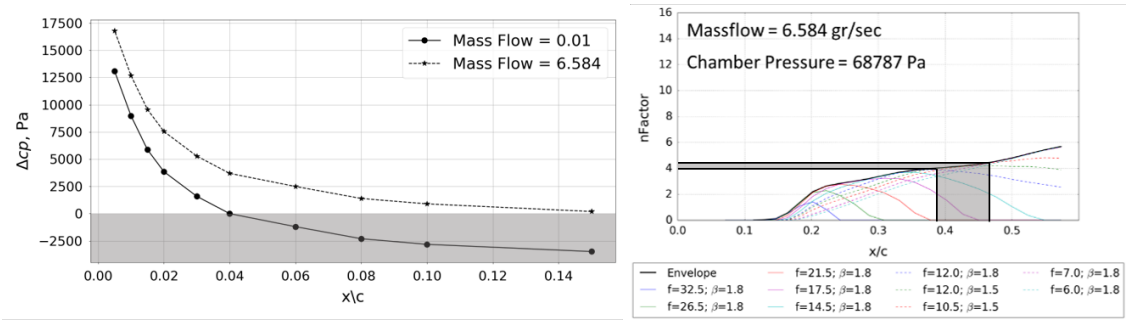

(c) Variable Porosity

Fig. 17 Linear Stability Analysis at Mach=0.7 and Angle of attack=-1.24

V. Non linear PSE (NL-PSE) on a selected case

A single case was analyzed with non-linear PSE using the experimental pressure distribution. The case selected is at $M = 0.7$ and angle of attack = 1°. The measured experimental transition location was ~ 40% chord-wise position. Initialization of a NL-PSE simulation, requires at the outset the identification of the most dominant disturbances that play a key role in the transition breakdown process. In the absence of this key input, we use a combination of tunnel noise data measurements coupled with the linear instability analysis to make some informed choices in this selection process.

Noise levels were measured during a previous wind tunnel test entry using the same model. In order to measure the noise a microphone was installed and supported from the ceiling of the tunnel, aligned fore-aft with the model center, external to the tunnel boundary layer (see Fig. 21). In addition to measurements using an in-flow microphone, disturbance measurements at the perforated wall were performed using a fast-response pressure transducer (Kulite).

As model incidence increased, the microphone broadband spectrum generally displayed an increase in sound power at frequencies above 6kHz (Fig. 22(a)). At frequencies below about 3kHz there was a general decrease. The frequencies of certain spectral features were modulated somewhat in an upward direction. This was valid at the selected Mach number.

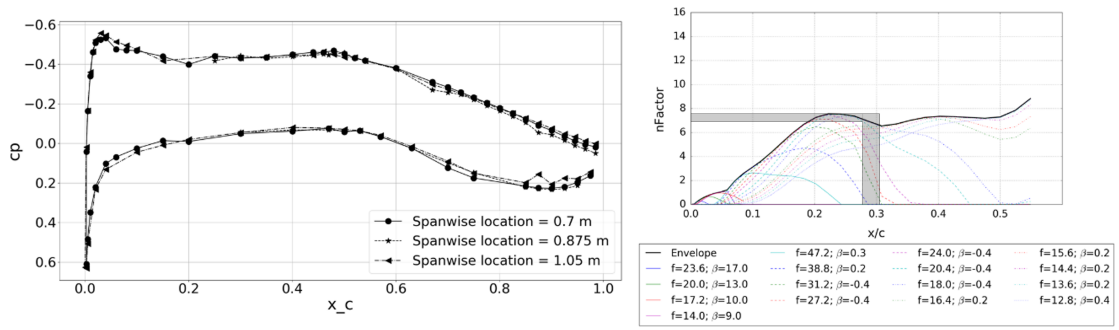

(a) Solid Cartridge

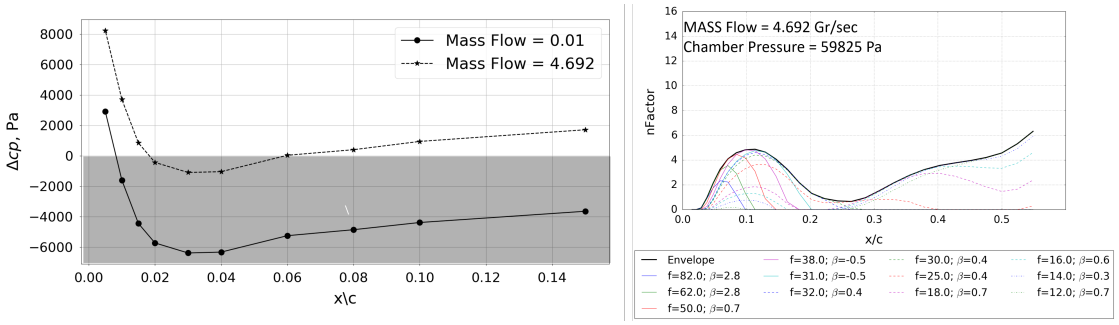

(b) Constant Porosity

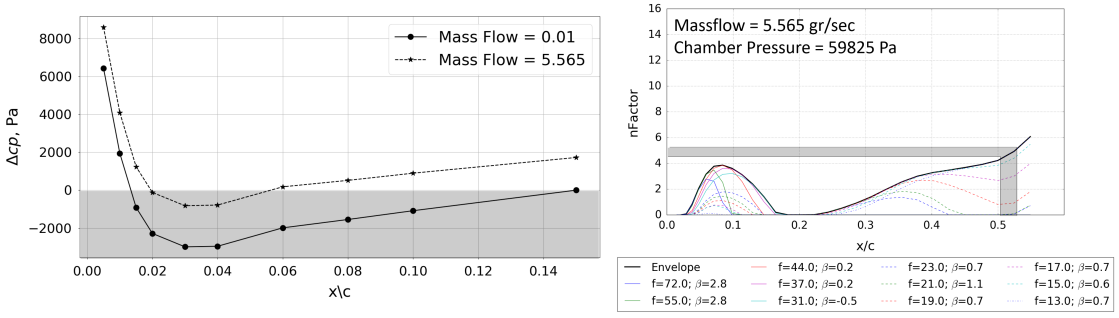

(c) Variable Porosity

Fig. 18 Linear Stability Analysis at Mach=0.7 and Angle of attack=1.82

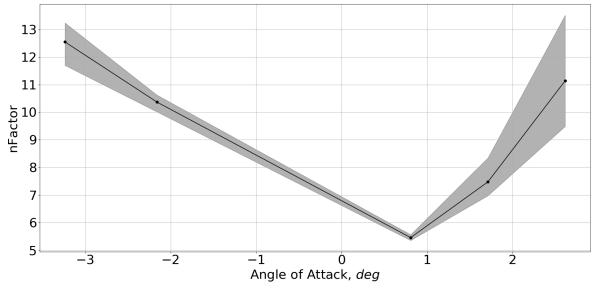

Fig. 19 Transition LPSE derived N-factor correlated with I-R.

Noise measured at the tunnel wall, which is assumed to be dominated by hydrodynamic content associated with the turbulent wall boundary layer, was considerably more powerful, as seen in the Kulite broadband characteristics

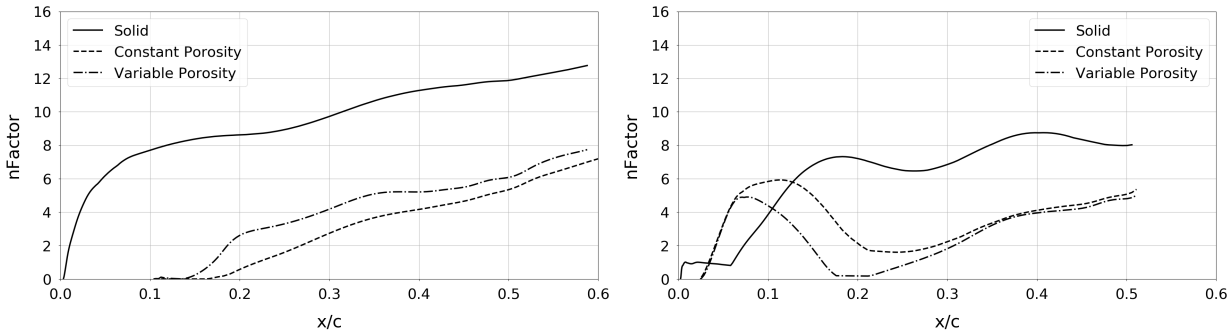

(a) Angle of attack=-1.24

(b) Angle of attack=1.82

Fig. 20 LPSE analysis at Mach=0.7

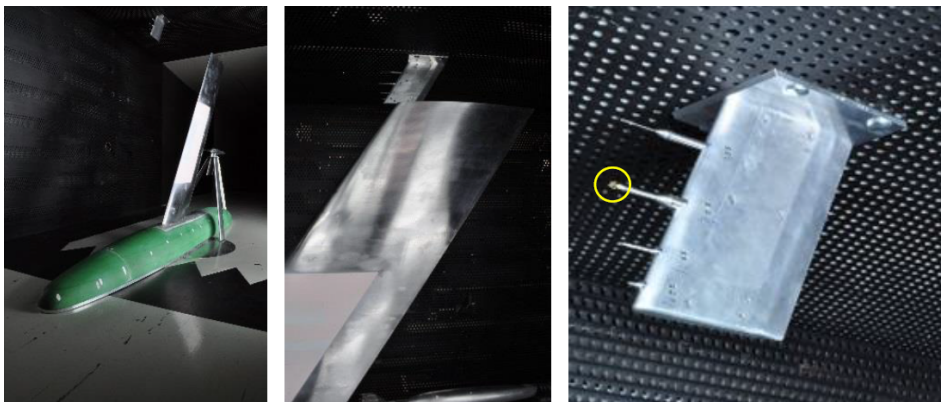

Fig. 21 Model an microphone configuration for the HLFC model. (in this view th microphone is replaced with and CTA probe, ringed)

(Fig. 22(b)). This was generally the case at all Mach numbers tested.

Looking at Fig. 23 the red symbols represent the overall envelopes of envelopes N-factors result generated with linear PSE. The blue dashed curve shows the evolution of the f=13kHz, β = 1000/m disturbance mode; the red dashed curve is the f=6.5 kHz, β = 1000/m case, while the black solid line is the f=6.5kHz result for all β's (envelope) with the β values considered ranged from β = 400/m to β = 2000/m. It is clear from the analysis to note that the f=6.5kHz disturbance is a non-player in the transition-breakdown event, even if the PSD shows a peak at this value. An important implication of this finding is that according to non-linear PSE this peak noise frequency present in the tunnel does *not* play an active role in the observed flow breakdown since the N-factor is significantly lower compared to N-factors of disturbances in the 13kHz frequency range.

The most dominant spanwise wavenumber from the linear analysis appears to be around the β = 1000/m value. Spanwise freestream turbulence scales were not available in the measured tunnel data. Thus the most that can be done, is to ascertain through a series of NL-PSE simulations the sensitivity of the results on varying the value of β in the simulations. In view of Fig. 22, in particular the wall based Kulite data relative to the freestream microphone measurements, indicate a slightly raised energy frequency spectra around the 13kHz range. So in an initial exploratory, and quite simplistic investigation, we investigate what the NL-PSE simulations indicate by scenarios based on disturbances forced around the β = 1000/m and frequencies around the 13kHz (ω) unknown parameter space.

Nonlinear PSE numerics and solution strategy are quite routine today, with numerous works outlining the basic method, so we do not dwell on this here (see for example Ref. [6, 7] for details). The nonlinear PSE (NL-PSE) is based on the ansatz

$$\hat{q}(x,y,z,t) = \bar{Q}(x,y) + \sum_{k=-K}^{k=+K} q_k(x,y) \exp\left(\int_{xo}^{x} i\alpha_k(s)\, ds + ik(\beta z - \omega t) \right). \tag{8}$$

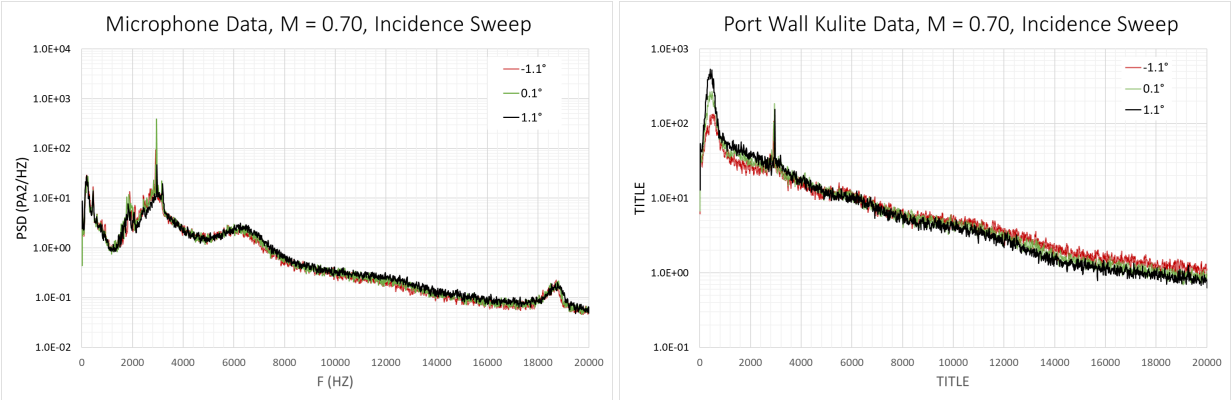

(a) Microphone data

(b) Wall Kulite data

Fig. 22 Noise data measured during the first HLFC test at M=0.7 for different angle of attack

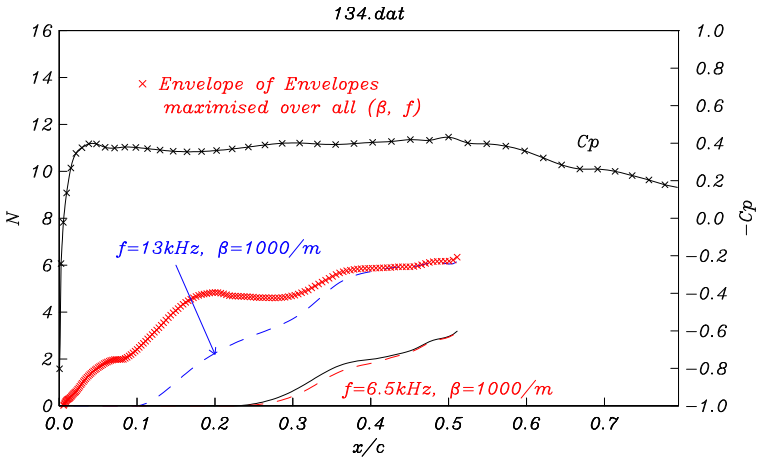

Fig. 23 Linear PSE analysis at 6500 Hz and 13000 Hz

Eqn. 8 mimics the pure oblique travelling CF wave nonlinear self-interaction scenario, for a given fundamental disturbance frequency ω and spanwise wavenumber β. In the above $\bar{Q}(x,y)$ represents the steady base flow computed by our boundary-layer solver (see Ref. [12]), while $q_k(x,y)$ represents the $k'th$ harmonic disturbance mode in the NL-PSE; $k = 0$ mode would thus represent the so-called $(0,0)$ mean-flow-distortion (mfd) steady flow correction to the $\bar{Q}(x,y)$ field, while q_1 in our notation represents the fundamental $(1,1)$ travelling CF mode used to initialize the NL-PSE simulations. The analysis we undertake is to prescribe an initial amplitude (u_{rms}) to the q_1-disturbance mode at an inflow data plane and then allow the NL-PSE simulations to self generate the higher harmonic modes through self-interaction.

The results of this sensitivity study are shown in Fig. 24. In each of the simulations, we arrange the initial forcing amplitude of the q_1-disturbance to have a magnitude of precisely $u_{rms} = 0.001$ at $x/c = 0.15$ – thus ensuring that some meaningful conclusions may be drawn based on *fixing* each simulation to have the identical *inflow* forcing magnitude for the various independent (β,ω) simulations. It is clear from Fig. 24 that the f=13kHz, $\beta = 1000$/m (and possibly the $\beta = 500$/m too) are the most destabilising disturbances, since saturated nonlinear states arise by about $x/c = 0.4$. Higher and lower frequencies are not as destabilizing, keeping the wavenumbers fixed; while simulations corresponding to the $\beta = 1500$/m disturbance are found to initially grow, but by about $x/c = 0.4$, they then reduce in amplitude. The $\beta = 500$/m simulations are interesting, in that in only a very narrow frequency space ~13kHz does a highly amplified saturated nonlinear state arise – the corresponding f=9kHz and f=18kHz simulations are predicted to be fairly benign.

In the results above, we specified the inflow magnitude of the fundamental forcing mode to have a magnitude of $u_{rms} = 0.001$ at $x/c = 0.15$, and selected the parameters $\beta = 1000$/m and f=13kHz based on the linear stability analysis.

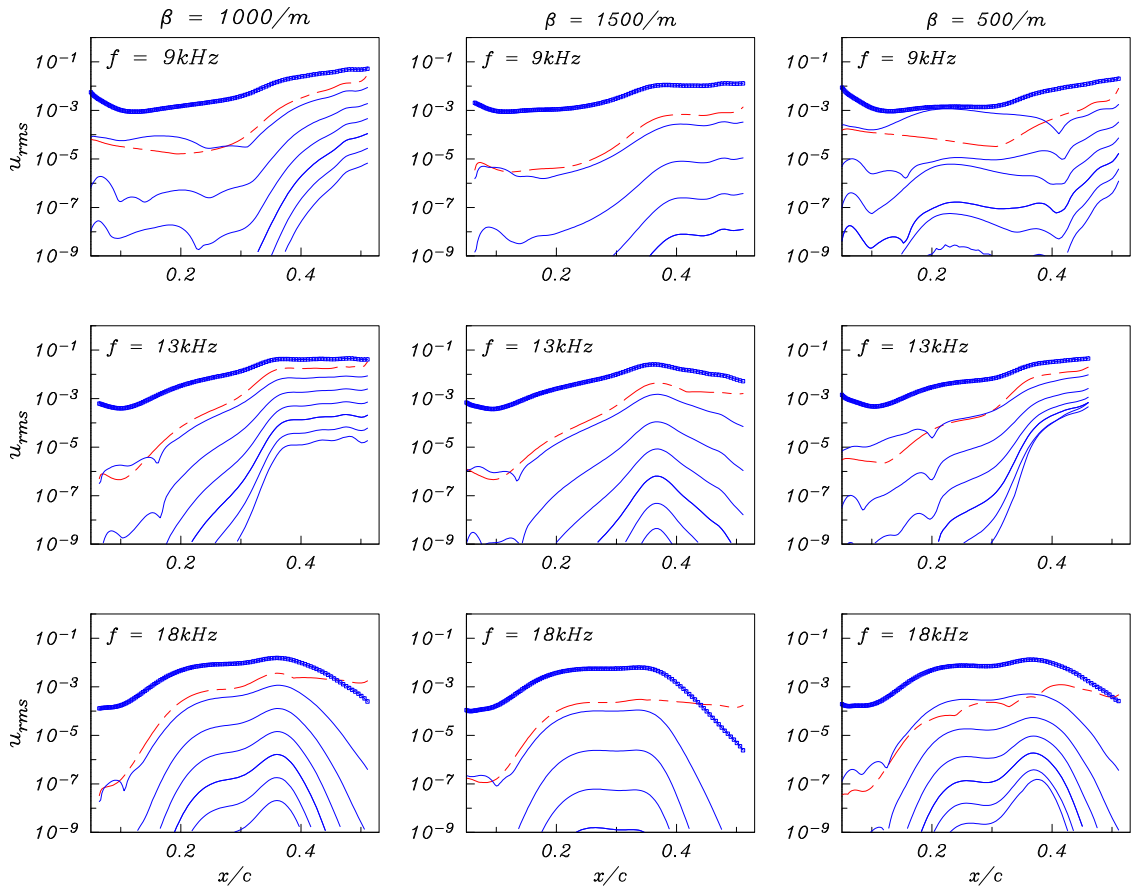

Fig. 24 Non-linear PSE analyses forced with different fundamental disturbances (β,ω). The thick solid curve represents the $(1,1)$ fundamental travelling forced CF mode; the red dashed curve represents the $(0,0)$ mfd mode; the remaining curves are the higher (k,k)-harmonics of the $(1,1)$ fundamental mode.

There were of course a number of unknowns in the experimental test campaign. The details necessary to enable NL-PSE simulations to more closely match the experiment, ultimately requires more detailed and accurate assessments of the freestream turbulence and acoustic spatial and frequency scales existing in the tunnel experimental test campaign. Moreover how the magnitudes of these same freestream fluctuations are entrained within the boundary-layer and give rise to generating disturbances and prescribing amplitudes within the boundary-layer are missing elements. Receptivity theory ([21], [22] suggests that not all fluctuations existing in the freestream lead to their counterpart disturbances being generated within the boundary-layer; only those that are in resonance with the naturally occurring eigenmodes pertaining to linear stability are generated and persist while convecting through the boundary layer. The analysis undertaken in this section was an exploratory look, to see whether some linkage with the limited tunnel environmental data and linear stability analysis, could be be used to ascertain and correlate findings with the observed I-R images of the transition front, in the nonlinear breakdown stages. This section, serves to highlight that a more correct and closer match with experimental findings will only arise, provided more detailed knowledge regarding the inflow state to *seed* nonlinear PSE simulations is available. It is our view that a future test campaign dedicated to making more detailed disturbance and tunnel environmental fluctuation measurements would provide considerable insight into the behaviour of the observed transition front and its changing character with incidence changes arising in Fig.'s 7 and 8.

VI. Conclusions

A complete analysis of the ARA HLFC test data has been performed. The analysis clearly shows that it is not possible to use a single N-factor. The N-factor is a function of the pressure distribution and does not only depend on the environment. The HLFC results allow additional observations:

- Linear stability can be used in ARA transonic wind tunnel at high sweep in the case of pure crossflow or pure T-S transition. In case of weak favourable gradient, linear stability fails to predict the transition location, underestimating the N-factor. The N-factor for crossflow and T-S is not a constant but a function of the angle of attack. This may be due to the limitations of the linear methods in case of interacting waves.
- Linear stability can be used as a design tool with HLFC systems. Measurement inside the cartridge will help to estimate the presence of blowing. Further work is required to estimate the N-factor on the HLFC system.
- Variable porosity shows a clear advantage in terms of suction pressure compared to constant porosity. In cases when the constant porosity failed to control transition, variable porosity was able to achieve better lower chamber pressure controlling transition.
- It was shown that it may be possible to stabilize the flow even in the presence of blowing with sufficient suction downstream of blowing.
- LPSE confirms the main findings of local linear stability analysis, both methods provide consistent results with and without suction. Preliminary work was performed using non-linear PSE, in the case selected it is shown how the peak noise source in the tunnel does not appear to be a factor in the observed transition trends. More work is required to understand the interaction between complex tunnel environmental forcing mechanisms and the transition front. A very simplistic nonlinear breakdown scenario is investigated in the current paper. It is hoped in future test campaigns, further more detailed measurements of the tunnel environment and fluctuations measured within the boundary-layer will enable more complex and realistic transition scenarios to be investigated.

Acknowledgments

The research leading to these results has received founding from the UK Department of Business, Energy & Industrial Strategy (BEIS) and Innovate UK (IUK).

References

[1] Allen, N., Lawson, S., Maina, M., and Alderman, J., "Qualification of the ARA TWT for laminar flow testing," *The Aeronautical Journal*, Vol. 118, No. 1209, 2014, pp. 1349, 1358.

[2] Ciarella, A., and Lawson, S., "Use of a Ring Wing Model to investigate Factors affecting Transition Measurement using Temperature Sensitive Paint and Hot Films in Transonic Flow," *55th AIAA Aerospace Sciences Meeting*, *AIAA Paper*: 2017-1217, Grapevine, Texas, 2017. URL https://doi.org/10.2514/6.2017-1217.

[3] Lawson, S., Ciarella, A., and Wong, P., "Development of Experimental Techniques for Hybrid Laminar Flow Control in the ARA Transonic Wind Tunnel," *2018 Applied Aerodynamics Conference*, *AIAA Paper*: 2018-3181, Atlanta, Georgia, 2018. URL https://doi.org/10.2514/6.2018-3181.

[4] Wong, P., and Walters, S., "Design and Performance Analysis of a Hybrid Laminar Flow Control (HLFC) Concept for a Civil Transport Aircraft," *Greener Aviation Conference*, Bruxelles, 2016.

[5] Wong, P. W. C., and Maina, M., "Flow Control Studies for Military Aircraft Applications," *AIAA 2nd Flow Control Conference*, *AIAA Paper*: 2004-2313, Portland, Oregon, 2004. URL https://doi.org/10.2514/6.2004-2313.

[6] Herbert, T., "Parabolized Stability Equations," *Annual Review of Fluid Mechanics*, Vol. 29, No. 1, 1997, pp. 245–283. URL https://doi.org/10.1146/annurev.fluid.29.1.245.

[7] Mughal, M. S., "Active Control of Wave Instabilities in Three- Dimensional Compressible Flows," *Theor. Comput. Fluid Dyn.*, Vol. 12, No. 4, 1998, pp. 195–217.

[8] Van-Ingen, J. L., *A Suggested Semi-empirical Method for the Calculation of the Boundary Layer Transition Region*, VTJ-74, VTH-74 TU Delft, 1956.

[9] Smith, A. M. O., and Gamberoni, N., *Transition, Pressure Gradient and Stability Theory*, ES26-388, Technical report ES-26388, Douglas Aircraft Company, 1956.

[10] Raposo, H., Mughal, S., and Ashworth, R., "Acoustic Receptivity and Transition Modeling of Tollmien-Schlichting Disturbances Induced by Distributed Surface Roughness," *Phys. Fluids*, Vol. 30, No. 4, 2018, p. 044105. URL https://doi.org/10.1063/1.5024909.

[11] Mughal, S. M., and Ashworth, R., "Uncertainty Quantification Based Receptivity Modelling of Crossflow Instabilities Induced by Distributed Surface Roughness in Swept Wing Boundary Layers," *43rd AIAA Fluid Dynamics Conference*, *AIAA Paper*: 2013-3106, San Diego, CA, 2013. URL https://doi.org/10.2514/6.2013-3106.

[12] Christian Thomas, C., Mughal, M. S., Gipon, M., Ashworth, R., and Martinez-Cava, A., "Stability of an Infinite Swept Wing Boundary Layer with Surface Waviness," *AIAA J.*, Vol. 54, No. 10, 2016. URL https://doi.org/10.2514/1.J054755.

[13] Thomas, C., Mughal, S., and Ashworth, R., "Development of Tollmien-Schlichting disturbances in the presence of laminar separation bubbles on an unswept infinite wavy wing," *Phys. Rev. Fluids*, Vol. 2, 2017, p. 043903. doi:10.1103/PhysRevFluids.2.043903, URL https://link.aps.org/doi/10.1103/PhysRevFluids.2.043903.

[14] Savitzky, A., and Golay, M. J. E., "Smoothing and Differentiation of Data by Simplified Least Squares Procedures," *Analytical Chemistry*, Vol. 36, No. 8, 1964, pp. 1427, 1639.

[15] Atkin, C., *User Guide for BL2D v3.4/v3.5*, Farnborough, 2014.

[16] Atkin, C., *User Guide for CoDS v5.6*, Farnborough, 2014.

[17] Mughal, S. M., "Stability Analysis of Complex Wing Geometries: Parabolised Stability Equations in Generalised Non-Orthogonal Coordinates," *36th AIAA Fluid Dynamics Conference and Exhibit*, *AIAA Paper*: 2006-3222, San Francisco, California, 2013. URL https://doi.org/10.2514/6.2006-3222.

[18] Mughal, M. S., *CoPSE/BL-MiPSecR User Manual: A Toolkit for Instability, Receptivity & Transition Analysis*, Imperial College, Internal report: Release 3.05.18, 2018.

[19] Poll, D. I. A., Danks, M., and Humphreys, B. E., "The Aerodynamic Performance of Laser Drilled Sheets," *1st European Forum on Laminar Flow Technology*, Vol. DGLR-Bericht 92-06, Hamburg, 1992.

[20] Preist, J., and Paluch, B., "Design Specification and Inspection of Perforated Panels for HLFC Suction Systems," *2nd European Forum on Laminar Flow Technology,*, Vol. DGLR-Bericht 92-06, Bordeaux, 1996.

[21] Ruban, A. I., "On Tollmien-Schlichting Wave Generation by Sound," *Laminar-Turbulent Transition*, edited by V. V. Kozlov, Springer Berlin Heidelberg, Berlin, Heidelberg, 1985, pp. 313–320.

[22] Goldstein, M. E., "Scattering of acoustic waves into Tollmien-Schlichting waves by small streamwise variations in surface geometry," *Journal of Fluid Mechanics*, Vol. 154, 1985, pp. 509–529. doi:10.1017/S0022112085001641.